THE JOURNAL OF BIOLOGICAL CHEMISTRY VOL. 289, NO. 46, pp. 32186–32200, November 14, 2014
© 2014 by The American Society for Biochemistry and Molecular Biology, Inc. Published in the U.S.A.

Molecular Mechanisms Associated with Xylan Degradation by *Xanthomonas* Plant Pathogens*

Received for publication, August 18, 2014, and in revised form, September 22, 2014 Published, JBC Papers in Press, September 29, 2014, DOI 10.1074/jbc.M114.605105

Camila Ramos Santos[‡1], **Zaira Bruna Hoffmam**[§1], **Vanesa Peixoto de Matos Martins**[‡1], **Leticia Maria Zanphorlin**[§], **Leandro Henrique de Paula Assis**[‡], **Rodrigo Vargas Honorato**[‡], **Paulo Sérgio Lopes de Oliveira**[‡], **Roberto Ruller**[§], **and Mario Tyago Murakami**[‡2]

From the [‡]*Biosciences National Laboratory and* [§]*Bioethanol Science and Technology Laboratory, National Center for Research in Energy and Materials, Campinas, São Paulo, 13083-970, Brazil*

Background: The xylanolytic activity is important for adaptation of *Xanthomonas* phytopathogen to the phyllosphere.
Results: XynB is a very efficient endo-xylanase activated by calcium ion, and XynA is a dimeric exo-oligoxylanase.
Conclusion: XynB degrades xylan, releasing xylooligosaccharides that are substrate for XynA.
Significance: This work elucidated the structural basis for the function of the xylanolytic enzymes from *Xanthomonas*.

***Xanthomonas* pathogens attack a variety of economically relevant plants, and their xylan CUT system (carbohydrate utilization with TonB-dependent outer membrane transporter system) contains two major xylanase-related genes, *xynA* and *xynB*, which influence biofilm formation and virulence by molecular mechanisms that are still elusive. Herein, we demonstrated that XynA is a rare reducing end xylose-releasing exo-oligoxylanase and not an endo-β-1,4-xylanase as predicted. Structural analysis revealed that an insertion in the β7-α7 loop induces dimerization and promotes a physical barrier at the +2 subsite conferring this unique mode of action within the GH10 family. A single mutation that impaired dimerization became XynA active against xylan, and high endolytic activity was achieved when this loop was tailored to match a canonical sequence of endo-β-1,4-xylanases, supporting our mechanistic model. On the other hand, the divergent XynB proved to be a classical endo-β-1,4-xylanase, despite the low sequence similarity to characterized GH10 xylanases. Interestingly, this enzyme contains a calcium ion bound nearby to the glycone-binding region, which is required for catalytic activity and structural stability. These results shed light on the molecular basis for xylan degradation by *Xanthomonas* and suggest how these enzymes synergistically assist infection and pathogenesis. Our findings indicate that XynB contributes to breach the plant cell wall barrier, providing nutrients and facilitating the translocation of effector molecules, whereas the exo-oligoxylanase XynA possibly participates in the suppression of oligosaccharide-induced immune responses.**

This is an open access article under the CC BY license.

Cell wall-degrading enzymes (CWDEs)[3] secreted by the type II secretion system (T2SS) are required for virulence and pathogenesis in the genus *Xanthomonas* (1–3). These enzymes such as xylanases, cellulases, and polygalacturonases degrade the main polysaccharides of plant cell walls, weakening the first physical barrier against pathogen attack and releasing nutrients during the colonization of plants (4–6). On the other hand, some CWDEs might have dual functions because their presence is sensed by plants, triggering defense responses (7). These enzymes can activate the innate immune system of plants by both pathogen-associated molecular patterns and damage-associated molecular patterns. In the pathogen-associated molecular pattern-triggered mechanism, CWDEs can elicit defense responses, independently of their enzymatic activity, as demonstrated for fungal xylanases (8, 9), which are recognized by specific receptors in the plant cell surface (10). In the damage-associated molecular pattern-triggered mechanism, the oligosaccharides produced by their enzymatic activity can activate the host innate immune system (11, 12) as demonstrated for plants pretreated with glycoside hydrolases, which showed enhanced resistance against pathogens (13). It is also proposed a functional interplay between the T2SS and type III secretion system (T3SS) in which the arsenal of CWDEs secreted by T2SS disrupts the plant cell wall integrity facilitating the translocation of effector proteins by T3SS (14, 15). Indeed, several T2SS genes from *Xanthomonas* spp. are coregulated with T3SS components supporting this model (14–16).

Interestingly, *Xanthomonas* pathogens contain a large repertoire of genes related to plant cell wall degradation and modification (at least 160 genes) that is equivalent to that observed in other bacteria specialized in biomass digestion such as *Ruminococcus albus* and *Clostridium cellulolyticum* (based on the CAZy database (17)). However, *Xanthomonas* spp. preferentially infect plants through stomata or lesions on leaves and

* This work was supported by grants from Fundação de Amparo à Pesquisa do Estado de São Paulo Grants 10/51890-8, 13/13309-0, and 14/07135-1; Conselho Nacional de Desenvolvimento Científico e Tecnológico Grants 476043/2011-5 and 308092/2012-0; and Coordenação de Aperfeiçoamento de Pessoal de Nível Superior.

The atomic coordinates and structure factors (codes 4PMU, 4PMV, 4PMX, 4PMY, 4PMZ, and 4PN2) have been deposited in the Protein Data Bank (http://wwpdb.org/).

[1] These authors contributed equally to this work.

[2] To whom correspondence should be addressed: Brazilian Biosciences National Laboratory, National Center for Research in Energy and Materials, Giuseppe Maximo Scolfaro 10000, 13083-970, Campinas/SP, Brazil. Tel.: 55-19-3512-1106; Fax: 55-19-3512-1100; E-mail: mario.murakami@lnbio.cnpem.br.

[3] The abbreviations used are: CWDE, cell wall-degrading enzyme; T2SS, type II secretion system; T3SS, type III secretion system; Xac, *Xanthomonas axonopodis* pv. *citri*; Xcc, *X. campestris* pv. *campestris*; Xoo, *X. orizae* pv. *orizae*; Xcv, *X. campestris* pv. *vesicatoria*; CE-LIF, capillary electrophoresis coupled to laser-induced fluorescence; RMSD, root mean square deviation; SAXS, small angle x-ray scattering.

other green parts, suggesting other functions to these enzymes that surpass the primary role in degrading cell wall polysaccharides (18, 19). The xylanolytic system, ubiquitous in lignocellulose-degrading microbes, is also found in *Xanthomonas* bacteria, playing important roles in virulence, biofilm formation, nutrient uptake and adaptation of these proteobacteria to the phyllosphere (3, 14, 20). This system, also known as xylan CUT (carbohydrate utilization with TonB-dependent outer membrane transporters) system in these phytopathogens, is composed by two major xylanase-related genes belonging to the GH10 family and other xylan-degrading enzymes such as β-xylosidases, arabinofuranosidases, acetyl xylan esterases, and α-glucuronidases (14). In *Xanthomonas axonopodis* pv. *citri* (Xac), the two xylanase-related proteins are encoded by the genes *xynA* (XAC4249) and *xynB* (XAC4254). It has been demonstrated that the gene *xynA* affects biofilm formation (21) and that orthologs in *Xanthomonas campestris* pv. *campestris* (Xcc) (20) and *Xanthomonas oryzae* pv. *oryzae* (Xoo) (3) do not display xylanase activity, despite the high sequence identity to classical endo-β-1,4-xylanases (~45–60%). In contrast, the divergent XynB, with maximum 30% of sequence identity to characterized GH10 xylanases, proved to be mainly responsible for the xylanase activity observed in Xoo (3) and Xcc (20). In Xoo, the corresponding *xynB* gene was shown to affect virulence and the complementation of a Δ*xynB* mutant strain with a clone containing *xynB* restored the lesion lengths to the WT levels (3). In *X. campestris* pv. *vesicatoria* (Xcv), the deletion of this gene also implicates in reduced extracellular xylanase activity and virulence (14).

Nevertheless, despite the importance of these GH10 xylanase-related proteins for the genus *Xanthomonas*, the molecular basis of their action on plant cell wall polysaccharides is not known. Thus, in an effort to better understand the xylanolytic system in these phytopathogens, we investigated the biochemical and structural properties of XynA and XynB from *X. axonopodis* pv. *citri*. Our results finely corroborate the *in vivo* studies, confirming the key role of XynB in degrading xylan chains from plant cell wall and demonstrating that XynA is involved in the breakdown of xylooligosaccharides, which might be elicitors of host defense responses (11, 12, 22). The elucidation of novel mechanisms implicated in xylan degradation by *Xanthomonas*, such as exo-oligoxylanase activity and calcium stimulation, expands our knowledge regarding the functional and regulatory repertoire within the GH10 family and also demonstrates the great potential of plant pathogen bacteria as a source of novel activities in the GH superfamily.

EXPERIMENTAL PROCEDURES

Molecular Cloning, Mutagenesis, and Protein Production—*xynA* and *xynB* were amplified from the genomic DNA of *X. axonopodis* pv. *citri* using standard cloning methods. Site-directed mutagenesis of *xynA* (L270R) was performed according to the QuikChange kit (Stratagene, La Jolla, CA), and the chimera containing the SVWNLPTAEVSTRFEYKPER sequence instead of LTKEGQIIGTGMAHKQFQLPEFKRFL was synthesized with the company GenScript (Piscataway, NJ). XynA, XynB, and mutants were expressed in BL21(DE3) cells supplemented with pRARE2 plasmid for 4 h at 30 °C with 0.5 mM isopropyl β-D-thiogalactopyranoside at $A_{600\ nm}$ of 0.6–0.8. The cells were collected, resuspended in lysis buffer (20 mM sodium phosphate, pH 7.5, 500 mM NaCl, 5 mM imidazole, 1 mM PMSF, and 5 mM benzamidine), and disrupted by lysozyme treatment (80 μg/ml, 30 min, on ice), followed by sonication. The target proteins were purified by immobilized metal ion affinity chromatography using a 5-ml HiTrap Chelating HP column (GE Healthcare), previously charged with Ni^{2+}, coupled to an ÄKTA purifier (GE Healthcare). The proteins were eluted using a nonlinear gradient (0–0.5 M) of imidazole at a flow rate of 2 ml/min. The eluted fractions were analyzed by SDS-PAGE, and those containing pure proteins were pooled, concentrated by filtration, and submitted to size exclusion chromatography. Size exclusion chromatography experiments were carried out at a flow rate of 1 ml/min using a HiLoad 16/600 Superdex 75-pg column (GE Healthcare), previously equilibrated with 20 mM sodium phosphate, pH 7.5, and 150 mM NaCl, coupled to an ÄKTA purifier (GE Healthcare). Sample homogeneity was evaluated by SDS-PAGE and dynamic light scattering.

Enzyme Assays and Carbohydrate Analyses—Activity assays were performed at 35 °C in 40 mM of sodium phosphate buffer (pH 6.0) for XynA (WT, L270R, and chimera) and 40 mM of MES buffer (pH 6.0) for XynB. The following substrates were tested: beechwood xylan (Sigma-Aldrich), rye arabinoxylan (Megazyme, Wicklow, Ireland), wheat arabinoxylan (Megazyme), larch arabinogalactan (Megazyme), sugar beet arabinan (Megazyme), lichenan (Megazyme), xyloglucan (Megazyme), xanthan gum (Sigma-Aldrich), mannan (Megazyme), laminarin (Sigma-Aldrich), β-glucan (Megazyme), and carboxymethylcellulose (Sigma-Aldrich). The amount of reducing sugar released from beechwood xylan (Sigma-Aldrich) was determined by the 3,5-dinitrosalicylic acid method (23). One unit is defined as the amount of enzyme that produces one μmol of reducing sugar per minute. To test the influence of calcium ion in the activity of XynB, the protein was incubated with 1 mM EDTA or preincubated with 1 mM EDTA for 30 min followed by addition of 10 mM $CaCl_2$. The apparent kinetic parameters K_m and V_{max} were calculated by nonlinear regression analysis of the Michaelis-Menten plot. L270R XynA, chimeric XynA, and XynB were used at final concentrations of 20, 1, and 2.5 ng/μl, respectively. In these experiments, the substrate concentration varied from 0.25 to 24 mg/ml. For capillary electrophoresis coupled to laser-induced fluorescence (CE-LIF), the reaction products of beechwood xylan (Sigma-Aldrich) or xylooligosaccharides (Megazyme) were derivatized with 8-aminopyrene-1,3,6-trisulfonic acid according to Chen and Evangelista (24). CE-LIF experiments were performed in a P/ACE MDQ instrument configured with a laser-induced fluorescence detection system (Beckman Coulter, Brea, CA). An uncoated fused silica capillary of 75-μm internal diameter and 20-cm effective length (Beckman Coulter, Brea, CA) was used for analysis of 8-aminopyrene-1,3,6-trisulfonic acid-labeled sugars. The capillary was conditioned with 0.1 M sodium phosphate (pH 2.5), and samples were injected by application of 0.5 p.s.i. for 5 s. Electrophoretic conditions were 20 kV/70–100 mA with reverse polarity at a controlled temperature of 25 °C. Oligosaccharides labeled with 8-aminopyrene-1,3,6-trisulfonic acid were excited at 488 nm, and emission was collected through a 520-nm band

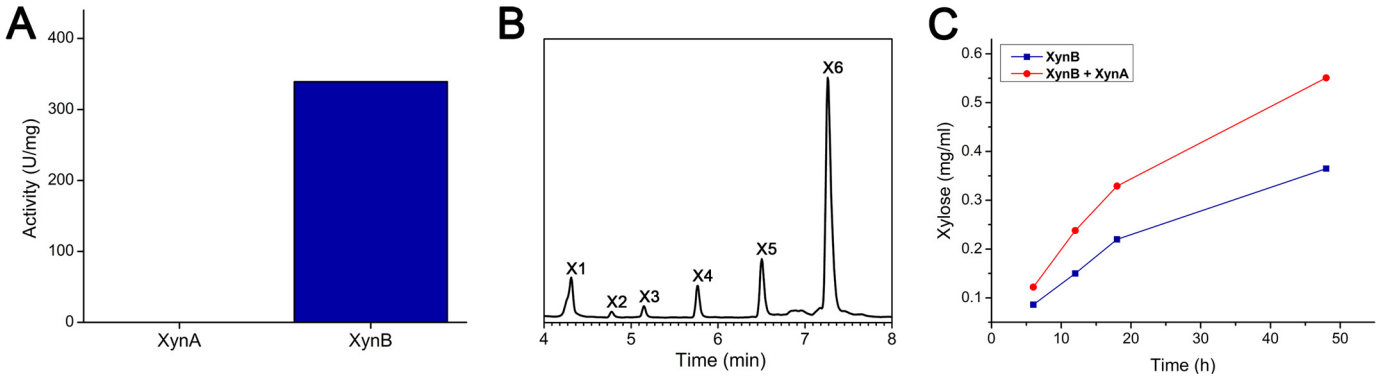

FIGURE 1. **XynA is an exo-oligoxylanase.** *A*, XynA and XynB activity against beechwood xylan. *B*, xylohexaose degradation by XynA analyzed by CE-LIF. *C*, xylose release from beechwood xylan using XynB or XynB complemented with XynA.

pass filter. The resultant peaks were assigned by comparison with electrophoretic behavior of standards: xylose (Sigma-Aldrich) and xylooligosaccharides (Megazyme). The xylooligosaccharides were quantitatively analyzed by high performance anion exchange chromatography using a Dionex ICS-3000 HPLC system equipped with a pulsed amperometric detector and a CarboPac PA-1 (4 × 250 mm) column. Samples were run with a flow rate of 0.5 ml/min, using a gradient from 100 to 500 mM NaOAc in 100 mM NaOH. The eluted peaks were compared with the retention time and concentrations of standard solutions of xylooligosaccharides (Megazyme) and xylose (Sigma-Aldrich).

Biophysical and Calorimetric Experiments—Far UV circular dichroism spectra were recorded on a Jasco J-815 spectropolarimeter (Jasco International Co., Ltd., Tokyo, Japan). Samples were prepared in 20 mM sodium phosphate, pH 7.5 (WT, L270R and Chimeric XynA), or 20 mM sodium cacodylate, pH 6.5 (XynB), at 10 μM. Unfolding experiments were monitored at 220 nm. For thermal denaturation experiments, the sample was heated at a rate of 1 °C/min over a temperature range of 20–90 °C. Differential scanning calorimetry measurements were performed on a VP-DSC microcalorimeter (MicroCal) using a heating rate of 1 °C/min in a temperature range of 20–90 °C. The protein concentration varied from 1.0 to 2.0 mg/ml for XynA, XynB, and mutants. XynB was analyzed in the presence of 5 mM EDTA or 5 mM $CaCl_2$ to assess the effect of calcium ions in protein stability. Sample scans were buffer-subtracted, concentration-normalized, and fitted by nonlinear least squares. The resulting excess heat capacity curves yielded the melting temperature (T_m) employed to compare thermal stability of the proteins and mutants. Isothermal titration calorimetry experiments of XynB with calcium ions were performed on a VP-ITC microcalorimeter (MicroCal) at 20 °C. Protein sample was extensively dialyzed against 20 mM sodium cacodylate, pH 6.5, and its concentration was set to 100 μM. The ligand solution was prepared to a final concentration of 1 mM. The affinity constant (K_a) were estimated from the best fit (one binding site) of the theoretical titration curve using the least squares fitting method. NITPIC software (25) was used for the integration of isothermal titration calorimetry data.

Small Angle X-ray Scattering—SAXS measurements for XynA, XynB, and mutants were performed at three different concentrations (2, 4, and 6 mg ml) in 20 mM Tris buffer, pH 7.5. Data were collected at both SAXS1 and SAXS2 Beamlines (Brazilian Synchrotron Light Laboratory, Campinas, Brazil). The integration of SAXS patterns was performed using Fit2D (26). Data were analyzed using the program GNOM (27). Molecular envelopes were calculated from the experimental SAXS data using the program DAMMIN (28). Ten runs of *ab initio* shape determination yielded highly similar models (normalized spatial discrepancy values of <1), which were then averaged using the package DAMAVER (29). The theoretical scattering curves of crystallographic structures were calculated and compared with the experimental SAXS curves using the program CRYSOL (30). The crystallographic structures were fitted into the corresponding SAXS molecular envelopes using the program SUPCOMB (31).

X-ray Crystallography—XynA was crystallized in two different space groups, $P2_1$ and $P4_32_12$, using the following solutions: 0.1 M Tris-HCl, pH 8.0, and 12% (w/v) polyethylene glycol 6000; and 0.1 M Tris-HCl pH 9.0, 6% (w/v) polyethylene glycol 6000, and 5% (v/v) glycerol, respectively. Crystals of XynB were obtained from a solution consisting of 0.05 M potassium dihydrogen phosphate and 14% (w/v) polyethylene glycol 8,000. The iodine derivative for XynB was prepared by soaking a single crystal in the reservoir solution containing 20% (v/v) glycerol and 0.5 M iodine chloride for 1 min. Complexes of XynB with X1, X2, and X3 were prepared by soaking the crystals into the mother solution containing 10 mM xylooligosaccharides (Megazyme) for 30 min. Diffraction intensities were measured in a CCD detector (MarMosaic225) at the MX2 Beamline (Brazilian Synchrotron Light Laboratory). The data were scaled and reduced using either HKL2000 (32) or XDS (33). XynA structure was directly solved by molecular replacement methods using the crystalline structure of the GH10 xylanase from *Cellvibrio mixtus* (Protein Data Bank code 1UQY; sequence identity of 45%) as template. The XynB structure was determined at 1.30 Å resolution by the single isomorphous replacement with anomalous scattering method using the programs SHELXD (34) and SHELXE (34) for heavy atom location and phase calculation, respectively. The model was further built with the AutoBuild wizard (35) from the PHENIX package yielding a nearly refined structure without internal gaps in the chain (96% complete) and crystallographic residuals (R) of 0.20 (R_{factor}) and 0.21 (R_{free}). All structures were refined with the program PHENIX.REFINE (36) and manually inspected using the pro-

TABLE 1
Data collection and refinement statistics of XynA and XynB structures

	XynA		XynB				
	Form I	Form II	Native	Iodine derivative	Xylose	Xylobiose	Xylotriose
Data collection							
Space group	$P2_1$	$P4_32_12$	$P2_12_12_1$	$P2_12_12_1$	$P2_1$	$P2_1$	$P2_1$
Cell dimensions							
a, *b*, *c* (Å)	87.02, 100.74, 134.20	78.83, 78.83, 303.98	49.05, 71.61, 83.46	49.46, 71.83, 83.84	71.85, 48.19, 77.76	72.06, 49.24, 83.04	49.28, 83.20, 72.05
α, β, γ (°)	90.0, 90.15, 90.0	90.0, 90.0, 90.0	90.0, 90.0, 90.0	90.0, 90.0, 90.0	90.0, 90.12, 90.0	90.0, 90.01, 90.0	90.0, 90.07, 90.0
Resolution (Å)	41.15–2.87 (2.92–2.87)	35.70–3.00 (3.05–3.00)	54.55–1.30 (1.32–1.30)[a]	31.87–2.00 (2.03–2.00)	41.01–1.60 (1.69–1.60)	42.39–1.40 (1.48–1.40)	27.47–1.42 (1.44–1.40)
R_{meas}	0.150 (0.610)	0.160 (0.704)	0.040 (0.561)	0.120 (0.323)	0.112 (0.692)	0.072 (0.730)	0.087 (0.556)
$I/\sigma I$	7.16 (1.62)	16.8 (3.8)	20.84 (1.87)	23.59 (6.94)	11.54 (2.55)	10.86 (1.66)	15.99 (2.91)
Completeness (%)	97.7 (95.9)	99.0 (97.4)	95.5 (94.4)	97.7 (95.8)	98.7 (96.5)	91.9 (91.4)	95.5 (93.6)
Redundancy	2.9 (2.6)	11.6 (10.4)	3.0 (2.9)	5.8 (5.8)	3.5 (3.5)	2.2 (2.1)	4.8 (4.5)
Heavy atom sites				21			
FOM[b]				0.74			
Refinement							
Resolution (Å)	41.15–2.86 (2.96–2.87)	48.14–3.00 (3.11–3.00)	54.55–1.30 (1.35–1.30)		41.01–1.60 (1.66–1.60)	42.39–1.40 (1.45–1.40)	27.47–1.40 (1.45–1.40)
No. reflections	52,253 (4,923)	19,572 (1,932)	68,888 (5,823)		69,577 (6,645)	112,589 (10,798)	104,741 (9,962)
R_{work}/R_{free}	0.2119/0.2626	0.2314/0.2533	0.1408/0.1841		0.1866/0.2291	0.1782/0.2069	0.1762/0.2282
No. atoms							
Protein	16,928	5,628	2,466		4,840	4,848	4,880
Ligand/ion	0	0	7		34	40	58
Water	91	23	331		275	579	565
Protein residues	2,131 (6 chains)	713 (2 chains)	306 (1 chain)		606 (2 chains)	606 (2 chains)	610 (2 chains)
Ligands			Ca^{2+}/GOL		Ca^{2+}/GOL/X1	Ca^{2+}/X2	Ca^{2+}/X3
B-factors (Å^2)							
Average	47.3	65.6	14.9		13.6	14.6	18.1
Protein	47.4	65.7	13.2		13.1	13.5	17.0
Ligand/ion			19.7		13.1	17.6	23.5
Water	25.8	41.5	26.9		21.6	23.0	26.8
RMSDs							
Bond lengths (Å)	0.005	0.005	0.024		0.007	0.005	0.020
Bond angles (°)	0.93	0.92	1.99		1.13	1.04	1.95
Ramachandran							
Favored (%)	96	96	98		97	97	97
Outliers (%)	0.05	0.28	0		0	0	0
Protein Data Bank code	4PMU	4PMV	4PMX		4PMY	4PMZ	4PN2

[a] The values in parentheses are for the highest resolution shell.
[b] Mean figure of merit computed for data to 1.3 Å and after density modification with program SHELXE.

gram COOT (37). The refined structures were evaluated using the program MolProbity (38). Data collection, processing, and refinement statistics are summarized in Table 1.

Computational Analysis—XynA (WT or mutants) and XynB (with or without calcium ion) structures were prepared for explicit solvent molecular dynamics simulations using the program YASARA (39) and the YAMBER3 force field. A simulation box was defined at 15 Å around all atoms of the structure. Protonation was performed based on pH 7. Cell neutralization was reached filling the box with water molecules and Na/Cl counter ions coupled with a short molecular dynamics simulation for solvent relaxation. Molecular dynamics simulations of 50 ns at 298 K were performed for each protein and root mean square deviations (RMSDs) were calculated for the whole structure and individual residues.

RESULTS

XynA Is a Rare Reducing End Xylose-releasing Exo-oligoxylanase—XynA exhibits significant sequence similarity to characterized endo-β-1,4-xylanases belonging to GH10 family such those from *C. mixtus* (CmXyn10B, 45%, Protein Data Bank code 1UQY (40)), *Bacillus stearothermophilus* (IXT6, 40%, Protein Data Bank code 2Q8X (41)), and *Paenibacillus barcinonesis* (PbXyn10B, 39%, Protein Data Bank code 3EMC (42)). However, biochemical analyses suggest that XynA is not an endo-β-1,4-xylanase because it is not able to hydrolyze xylan chains (Fig. 1*A*). This result is in agreement with *xynA* mutant strains of both Xcc (20) and Xoo (3) in which secreted xylanase activity was similar to that observed for the WT strains, indicating that the xylanase activity is not conferred by *xynA* orthologous genes. Interestingly, enzymatic assays revealed that XynA was able to hydrolyze xylohexaose (X6) (Fig. 1*B*) and shorter xylooligosaccharides (results not shown) in an exo manner. The enzyme produced mainly xylopentaose (X5) and xylose (X1) from X6, which is distinctive for an exo-acting enzyme (Fig. 1*B*). Moreover, the xylan hydrolysis by the endo-xylanase XynB (discussed later) complemented with XynA increased in ~50% the xylose production (Fig. 1*C*), which corroborates with the ability of XynA to release xylose from xylooligosaccharides. These analyses demonstrate that XynA is an exo-oligoxylanase and not an endo-xylanase as expected by sequence similarity analysis.

To understand the structural determinants for the exo-oligoxylanase activity of XynA, its crystallographic structure was determined in two different space groups (Table 1): $P4_32_12$ and $P2_1$. In both cases, a stable dimeric arrangement with a buried area of 1972 Å^2 and a ΔG^{int} of −8.8 kcal/mol was found (Fig. 2). In tetragonal crystals, one dimer is present in the asymmetric unit, whereas three dimers are found per asymmetric unit in monoclinic crystals. SAXS and dynamic light scattering analyses also supported the biological unit of XynA as a dimer in solution (Fig. 3). This quaternary configuration is principally stabilized by the loop connecting the topological elements β7 and α7 (Fig. 4). This loop comprises the sequence VLPLT**KE**GQIIGTGMAH**K**QFQLP**E**F**KR**FL**D**PY**RD**GLPA**D** (hydrophobic and charged residues are underlined or in bold, respectively) and is swapped between the two subunits establishing a number of hydrophobic and ionic interactions (Fig. 2 and Table 2). A cluster of three aromatic residues (Phe^{286}, Phe^{291}, and Phe^{294}) forms the hydrophobic core of the interface, whereas three electrostatic interactions are present in the solvent-exposed region (Glu^{290}–Arg^{204}, Asp^{158}–Lys^{284}, and Glu^{273}–Arg^{293}) (Fig. 2). Sequence alignment showed that all residues considered relevant for catalysis and substrate recognition are conserved in XynA, except the β7-α7 loop that is only observed in

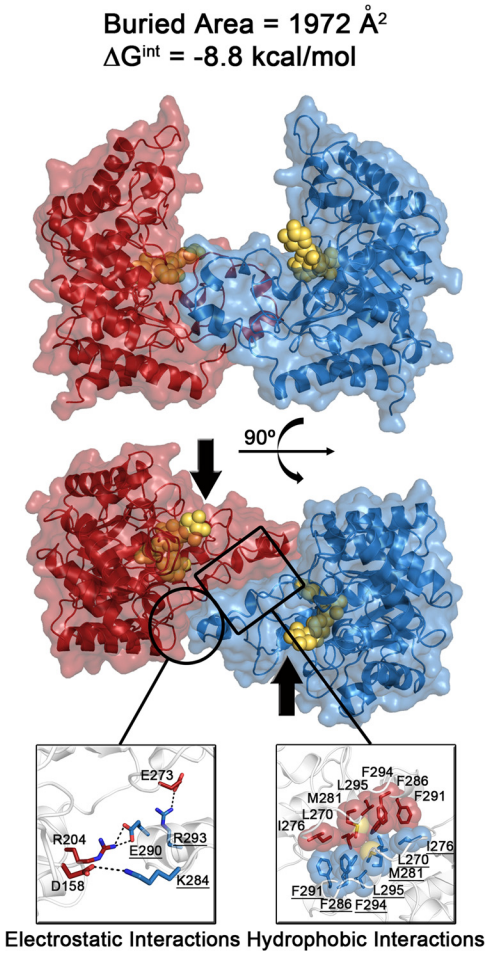

FIGURE 2. **Structure of the XynA dimer.** Different views of the dimer, highlighting the hydrophobic and electrostatic interactions involved the stabilization of the interface. These interactions are detailed in Table 2. The active sites are indicated by the *arrows*. The xylooligosaccharides were modeled in the catalytic cleft of XynA (−3 to +1 subsites) based on the structure of CmXyn10B (Protein Data Bank code 1UQY (40)) and are represented by *yellow spheres*.

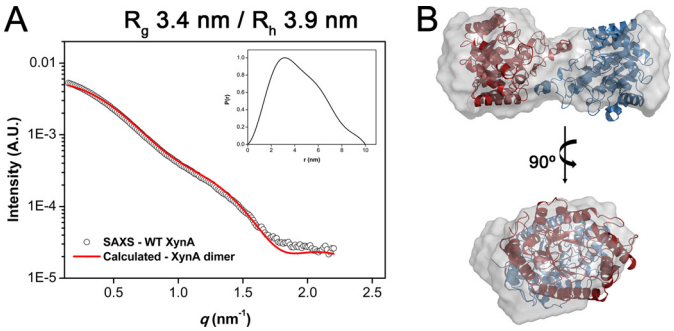

FIGURE 3. **SAXS analysis of XynA.** *A*, experimental scattering curve and calculated theoretical curve for the crystallographic dimer. *Inset*, normalized distance distribution function. *B*, the crystallographic dimer fitted into the low resolution envelope is shown in two different views.

XynA orthologs from the genus *Xanthomonas* (Fig. 4). The U-shaped architecture of the dimer with the active sites of both subunits facing each other (Fig. 2) implicates in a physical barrier of the aglycone region by this $\beta7$-$\alpha7$ loop (Fig. 5*A*).

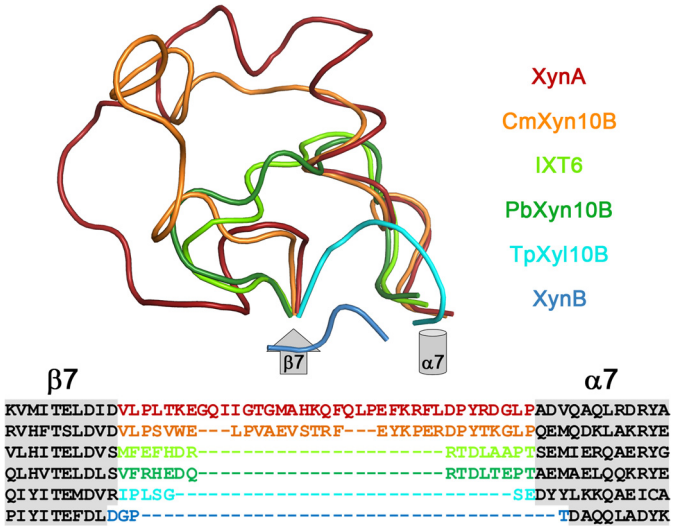

FIGURE 4. **Architecture and amino acid composition of the $\beta7$-$\alpha7$ loop from structurally characterized GH10 enzymes.** XynA (Protein Data Bank code 4PMV; this work), CmXyn10B (Protein Data Bank code 1UQY (40)), IXT6 (Protein Data Bank code 2Q8X (41)), PbXyn10A (Protein Data Bank code 3EMC (42)), TpXyl10B (Protein Data Bank code 3NIY (48)), and XynB (Protein Data Bank code 4PMX; this work).

Structural comparison with GH10 endo-β-1,4-xylanases complexed with xylooligosaccharides revealed that the −2, −1, and +1 subsites are highly conserved (Figs. 5 and 6). However, the $\beta7$-$\alpha7$ loop in XynA obstructs the remaining aglycone-binding subsites. The +2 subsite is fully blocked with a glutamine residue occupying the corresponding position of the glycosyl moiety in this subsite (Fig. 5*C*). The further +3 and +4 subsites are fulfilled by the main chain of the $\beta7$-$\alpha7$ loop from the other subunit (Fig. 5, *A* and *C*). This finding along with its exo cleavage pattern suggests that XynA releases a xylose unit from the reducing end of the substrate. This mode of action was only observed so far in a GH8 enzyme from *Bacillus halodurans* C-125 (Rex) (43). As observed for XynA, the catalytic machinery of Rex is conserved when compared with endo-type GH8 enzymes, but the +2 subsite is sterically blocked by a kink in the loop preceding the $\alpha10$ helix (44). In Rex, the residue His^{319} forms a hydrogen bond with the β-hydroxyl group of xylose at the +1 subsite, contributing to the specificity of the reducing end (44). By analogy, the residue Gln^{260} seems to play an equivalent role in XynA based on its geometry and comparative studies with other xylanase-oligosaccharide complexes. Our experimental findings combined with the notable similarity to the mechanism described for Rex strongly indicate that XynA is a reducing end xylose-releasing exo-oligoxylanase.

TABLE 2

Intermolecular side chain-side chain and main chain-side chain interactions of the XynA dimeric interface

The molecules A and B, present in the asymmetric unit of the $P4_32_12$ crystal (Protein Data Bank code 4PMV), were used for interface analysis with the Protein Interaction Calculator (67).

HYDROPHOBIC INTERACTIONS						ELECTROSTATIC INTERACTIONS					
Nº	RES	CHAIN	Nº	RES	CHAIN	Nº	RES	CHAIN	Nº	RES	CHAIN
270	Leu	A	294	Phe	B	158	Asp	A	284	Lys	B
270	Leu	A	291	Phe	B	273	Glu	A	293	Arg	B
270	Leu	A	270	Leu	B	290	Glu	A	204	Arg	B
270	Leu	A	295	Leu	B	204	Arg	A	290	Glu	B
276	Ile	A	291	Phe	B	284	Lys	A	158	Asp	B
276	Ile	A	286	Phe	B	293	Arg	A	273	Glu	B
281	Met	A	281	Met	B						
281	Met	A	286	Phe	B						
286	Phe	A	270	Leu	B						
286	Phe	A	276	Ile	B						
291	Phe	A	270	Leu	B						
291	Phe	A	276	Ile	B						
294	Phe	A	270	Leu	B						
294	Phe	A	294	Phe	B						
295	Leu	A	270	Leu	B						

HYDROGEN BONDS											
Nº	CHAIN	RES	ATOM	Nº	CHAIN	RES	ATOM	Dd-a[1]	Dh-a[2]	A(d-H-N)[3]	(a-O=C)[4]
277	A	Ile	N	285	B	Gln	OE1	2.85	1.89	165.73	114.19
277	A	Ile	N	285	B	Gln	NE2	3.45	2.67	136.61	82.85
285	A	Gln	NE2	277	B	Ile	O	2.76	1.79	151.44	146.37
285	A	Gln	NE2	277	B	Ile	O	2.76	3.33	48.60	146.37
293	A	Arg	NH2	273	B	Glu	O	3.43	3.19	94.08	139.06
293	A	Arg	NH2	273	B	Glu	O	3.43	2.90	112.64	139.06
277	B	Ile	N	285	A	Gln	OE1	2.83	1.89	157.29	123.13
285	B	Gln	OE1	275	A	Gln	O	3.49	3.37	87.01	123.25
285	B	Gln	OE1	275	A	Gln	O	3.49	3.06	105.10	123.25
285	B	Gln	NE2	277	A	Ile	O	2.80	1.88	143.39	134.58
285	B	Gln	NE2	277	A	Ile	O	2.80	3.22	56.89	134.58

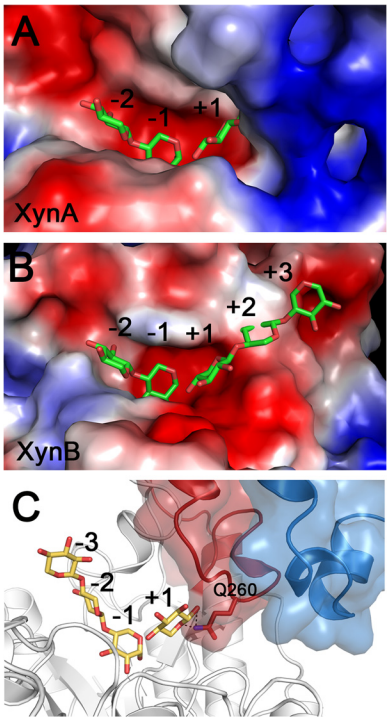

FIGURE 5. **Dimerization loop (β7-α7 loop) blocks the +2 subsite of XynA.** *A* and *B*, electrostatic surface potential of XynA (*A*) and XynB (*B*). *C*, the residue Gln^{260}, present in the β7-α7 loop, probably participates in the recognition of the xylosyl group at the +1 subsite of XynA. The xylooligosaccharide shown in *A–C* was modeled in the active site of XynA (*A* and *C*) and XynB (*B*) based on the structure of CmXyn10B (Protein Data Bank code 1UQY (40)).

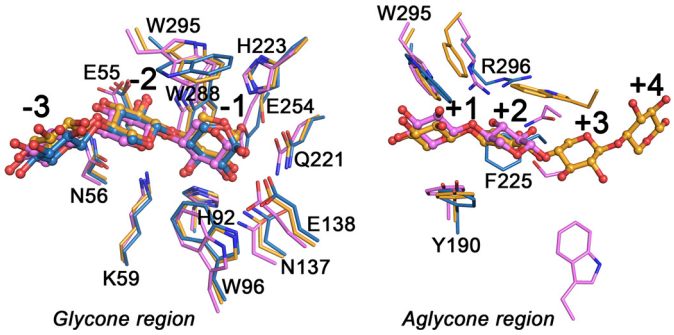

FIGURE 6. **Glycone- and aglycone-binding regions of XynB (*blue*), CmXyn10B (*yellow*), and SoXyn10A (*pink*).** The oligosaccharides shown are from the complex structures of XynB (Protein Data Bank code 4PN2; this work), CmXyn10B (Protein Data Bank code 1UQY (40)), and SoXyn10A (Protein Data Bank code 1ISV (47)). The same colors were used for the protein and the carbohydrate molecules of each complex.

Tuning the Action Mode of XynA by Rational Redesign of the β7-α7 Loop—To examine the role of the β7-α7 loop and the quaternary structure in the action mode of XynA, a single mutant (L270R) and a chimera replacing this loop by a conserved sequence observed in typical endo-β-1,4-xylanases were produced and characterized. The mutation L270R was sufficient to disassemble the dimer because the Arg residue was inserted into the hydrophobic core of the interface promoting repulsive forces and steric impediments (Fig. 7, *A* and *B*). The L270R mutant catalyzed the hydrolysis of xylan chains (Fig. 8*A* and Table 3); however, with low catalytic efficiency compared with XynB (Table 3). The cleavage pattern was also altered against xylooligosaccharides, resembling a profile of hydrolysis observed for endo-β-1,4-xylanases, with the predominance of X3 and X2 as final products (Fig. 8*A*). These data confirm that the single mutation, and consequently the disruption of the dimeric arrangement, was sufficient to change the action mode of XynA. Remarkably, the chimeric XynA showed 20-fold higher catalytic efficiency than the L270R mutant and 15% higher than XynB (Table 3). This catalytic efficiency is at least 7-fold higher than that observed for other mesophilic GH10 xylanases such as CmXyn10B (40), Xyn10A from *Bacteroides xylanisolvens* (45), and XynA from *Glaciecola mesophila* (46). Kinetic data revealed a notable improvement of both K_m and V_{max} in comparison with the single mutant (Table 3). CE-LIF analysis confirmed that the loop replacement fully converted XynA into a classical endo-acting enzyme producing X2 and X3 from xylan and X6 (Fig. 8*B*). SAXS data demonstrated the monomeric form of the chimeric XynA in solution (Fig. 7, *C* and *D*), supporting the importance of accessibility to positive subsites for the development of endo-xylanase activity. Moreover, the chimeric enzyme showed a broad pH plateau for activity ranging from 6 to 9 and optimum temperature of 35 °C. These biochemical properties along with the stunning catalytic performance make this tailored enzyme a potential biocatalyst for biotechnological processes at moderate temperatures. In addition to the changes in functional behavior, the mutations also affected the structural stability of XynA. The L270R mutant had a 10 °C reduction in the melting temperature as assessed by differential scanning calorimetry (Fig. 9*A*) and circular dichroism (Fig. 9*B*), whereas the chimeric XynA presented a decrease of ~6 °C (Fig. 9, *A* and *B*). In accordance with thermal denaturation experiments, molecular dynamics simulations also showed lower overall RMSD values for WT in comparison with mutants. These biophysical and computational analyses converge to the dimeric arrangement as the most stable form of XynA, which is expected because of the key role played by dimerization in the functional expression of this enzyme. Collectively, these results confirm the essential role of the β7-α7 loop in governing the action mode of XynA and also confirm its reducing end xylose-releasing exo-oligoxylanase activity.

The Divergent XynB Is an Endo-β-1,4-xylanase—XynB shows low sequence identity to characterized endo-β-1,4-xylanases (≤30%) such those from *Streptomyces olivaceoviridis* (SoXyn10A, 30%, Protein Data Bank code 1ISV (47)), *Thermotoga petrophila* (TpXyl10B, 28%, Protein Data Bank code 3NIY (48)), *C. mixtus* (CmXyn10B, 26%, Protein Data Bank code 1UQY (40)), and *B. stearothermophilus* (IXT6, 23%, Protein Data Bank code 2Q8X (41)). However, functional studies with Δ*xynB* strains of Xcc (20), Xoo (3), and Xcv (14) revealed a major role of this gene in the expression of extracellular xylanase activity. Based on these observations, we analyzed biochemical and structural properties of XynB to elucidate the structural basis for its functional behavior despite the low identity to classical GH10 xylanases. Biochemical analyses confirmed that XynB is a *bona fide* xylanase being active against both xylan and xylooligosaccharides (Fig. 8*C*). The enzyme showed a broad pH range for activity and an optimum temperature of 35 °C, as observed for the chimeric XynA. Different substrates were tested, and similarly to classical xylanases,

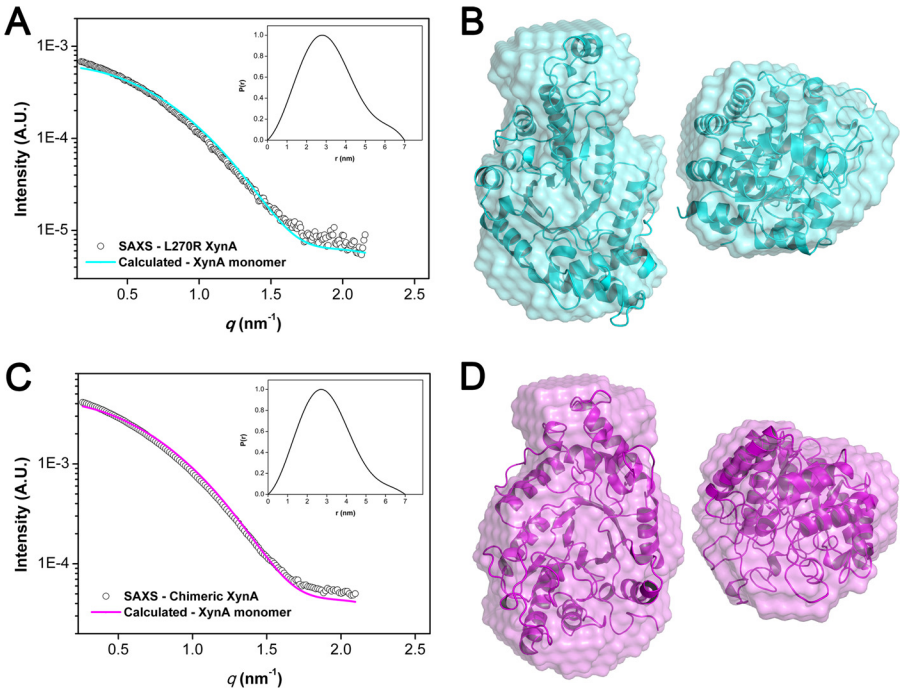

FIGURE 7. **SAXS analysis of L270R and chimeric XynA.** *A* and *C*, experimental scattering curves and calculated scattering curves for the monomeric models of L270R (*A*) and chimeric XynA (*C*). *Insets*, normalized distance distribution functions. *B* and *D*, the monomeric models were fitted into the low resolution envelopes of L270R (*B*) and chimeric (*D*) XynA.

XynB can only degrade xylose-based substrates. XynB has a preference for linear xylan (beechwood xylan), but also hydrolyzed decorated polymers (wheat and rye arabinoxylans), mainly those containing monosubstituted xylosyl residues (Table 4). Interestingly, XynB was strongly inhibited by chelating agents (Fig. 10*A*), indicating a dependence for divalent ions. Indeed, crystallographic and calorimetric studies (as discussed later) showed the ability of XynB to bind calcium ions. Thus, kinetic parameters were determined against beechwood xylan for the enzyme as purified and with the addition of $CaCl_2$ (Table 3). The addition of calcium ions was to guarantee that all calcium-binding sites are occupied, and the enzyme is fully active. Under such conditions, XynB presented an apparent K_m of 2.4 mg/ml and V_{max} of 1300 units/mg (Table 3), yielding a catalytic efficiency of 339 ml/mg·s, highlighting the importance of calcium ion for enzymatic activity. The cleavage pattern of xylan and xylohexaose by XynB revealed X2, X3, and X4 as the main products (Fig. 8*C*), suggesting an endo mode of action. However, the release of small amounts of xylose in these reactions (Fig. 8*C*) indicates that XynB is not a strict endo-acting enzyme. Although it is not expected for a typical endo-acting enzyme, similar results have been observed for other GH10 xylanases (49–51). These results support that XynB is the major xylanolytic enzyme from the xylan CUT system, in accordance with *in vivo* studies in Xoo (3), Xcc (20), and Xcv (14).

The crystallographic structure of XynB, determined by the single isomorphous replacement with anomalous scattering method (Table 1), revealed a canonical $(\beta/\alpha)_8$ topology with the major structural differences in relation to other characterized GH10 xylanases in the loops forming the catalytic interface, particularly at the aglycone-binding region (Fig. 11). Inspection of electron density maps indicated the presence of an ion in the vicinity of the catalytic cleft, and analysis of bond distances, coordination geometry, B factor, and difference maps (52) indicated that the most likely ion is calcium, as supported by functional and calorimetric studies. Xylose (X1) and xylooligosaccharides (X2 and X3) complexes were also solved at high resolution (Fig. 12) showing conserved −3, −2, and −1 subsites (Fig. 6), as reported in previous crystallographic studies with GH10 xylanases (40, 47, 48, 53). It is worthy of mention that the xylosyl moiety occupying the −3 subsite is not contacting any protein residue with its orientation determined by steric impositions of the glycosidic bond within the trisaccharide (Fig. 12). The same binding mode of X3 was observed for CmXyn10B and SoXyn10A (Fig. 6), indicating that the −3 subsite does not seem productive for substrate recognition and binding. Interestingly, the −2 and −1 subsites are also conserved in the reducing end xylose-releasing exo-oligoxylanase (XynA) reported here, which reveals a high degree of conservation of the subsites involved in the glycone recognition. Based on that, it is possible to conclude that the negative subsites are not the basis for the functional diversity within the GH10 family.

In contrast to the glycone-binding region, the positive subsites are very divergent in terms of geometry and physicochemical properties. Even the +1 subsite, which should be conserved as a minimal requirement for the recognition and subsequent cleavage of the β-1,4 bonds between xylosyl moieties, contains significant differences in the interaction network supporting the substrate binding. Two aromatic residues are fully conserved (Tyr^{190} and Trp^{295}); however, XynB has a positively charged residue (Arg^{296}) also forming the +1 subsite, whereas in CmXyn10B, it is replaced by a hydrophobic residue (Phe^{340}) (Fig. 6). The +2 subsite in SoXyn10A is exclusively based on polar interactions involving Asn^{209}, Ser-, and Arg^{275}, whereas

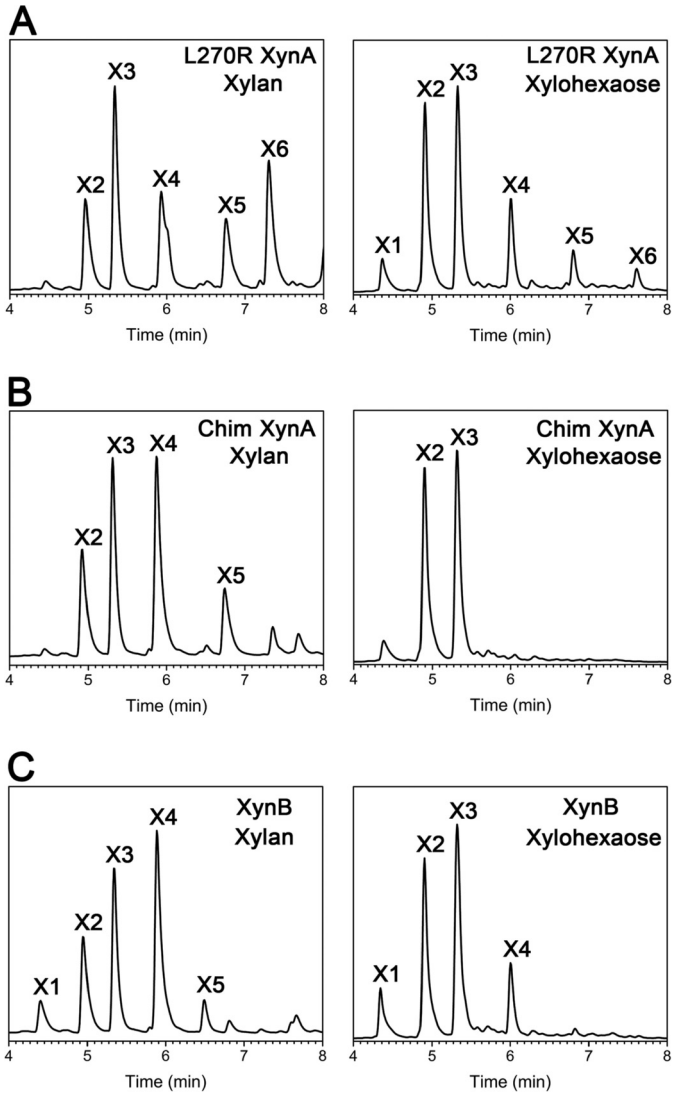

FIGURE 8. **Capillary electrophoretic analysis of xylan and xylohexaose (X6) hydrolysis by L270R XynA (*A*), chimeric XynA (*B*), and XynB (*C*).**

TABLE 3

Apparent kinetic parameters of L270R XynA, chimeric XynA and XynB using beechwood xylan as substrate

Parameter	L270R XynA	Chimeric XynA	XynB As purified	XynB With Ca^{2+}
V_{max} (units mg^{-1})	185 ± 0.3	2400 ± 0.1	1400 ± 0.2	1300 ± 0.1
K_m (mg ml^{-1})	6.7 ± 0.8	4.3 ± 0.4	4.5 ± 0.5	2.4 ± 0.2
k_{cat} (s^{-1})	134 ± 19	1682 ± 188	870 ± 111	801 ± 69
k_{cat}/K_m (s^{-1} mg^{-1} ml)	20 ± 4	391 ± 59	195 ± 34	339 ± 40

in XynB, an aromatic residue (Phe^{225}) replaces the two polar residues, Asn^{209} and Ser^{212} (Fig. 6). In CmXyn10B, the +2 subsite comprises basically of a tryptophan residue, but it is located at the opposite side of Phe^{225}. Because of the large variance in the further positive subsites among structurally characterized GH10 xylanases, it was not possible to map the residues forming these subsites in XynB. CmXyn10B exhibits an extended $\beta7$-$\alpha7$ loop, the same related to the functional behavior of XynA, that contributes to the formation of the +2, +3, and +4 subsites (Fig. 11*C*) and SoXyn10A has also a +5 subsite formed by a tryptophan residue (Trp^{179}) (Fig. 11*C*). In XynB, both motifs are absent, and the fully conserved region comprising the segment Val^{136}–Trp^{166} adopts a very different conformation, yielding a broadened active site, which may explain the ability of XynB to degrade decorated xylan chains (Fig. 11*B*). These observations along with XynA findings clearly indicate that the distinct architectures of the positive subsites are intimately associated to the functional behavior of GH10 enzymes in terms of catalytic efficiency, mode of action, and substrate recognition.

Calcium Ion Is Essential for Function and Stability of XynB—Biochemical studies demonstrated a strong inhibitory effect of chelant agents on XynB activity, which indicates a role of divalent ions on the enzyme function. Indeed, XynB not only recovered but increased 10-fold its catalytic activity by the complementation with calcium ions after EDTA treatment (Fig. 10*A*). The enzyme was also responsive to magnesium, but in a lesser extent, whereas other metal ions did not induce the recovery of xylanase activity. We also interrogated the importance of this ion for protein stability, and both differential scanning calorimetry (Fig. 10*B*) and circular dichroism (Fig. 10*C*) techniques showed a remarkable stabilization in the protein structure (ΔT_m = +11 °C) by calcium ions. These results support that both structural stability and function of XynB are affected by calcium ions. To date, only the enzyme CjXylA showed a stabilizing effect induced by calcium ions (ΔT_m = +6 °C) (50) within the GH10 family. However, the ion binding to CjXylA did not influence the catalytic activity (50), suggesting that this dual effect is unique to XynB. Furthermore, the affinity of calcium ions to XynB was calorimetrically measured, indicating a K_a of 4.7×10^4 M^{-1} and one calcium-binding site per monomer (Fig. 13*A*). This affinity is quite similar to that observed for calcium binding to CjXylA (K_a of 4.9×10^4 M^{-1}) (50), despite the fact that the binding sites are totally different (Fig. 13*B*). The crystallographic structure of XynB revealed that the calcium ion binds to an N-terminal motif between the $\beta2$-$\alpha2$ loop and $\alpha3$ helix that is located at the opposite side of the catalytic interface in comparison with the calcium-binding site of CjXylA (Fig. 13*B*). This ion is caged into an O_6 octahedral coordination sphere formed by the side chains of the residues Glu^{64}, Asp^{68}, Glu^{115}, and Gln^{118}, and two solvent molecules (Fig. 13*B*). These residues are not conserved in other GH10 members, indicating them to be a unique calcium-binding site to XynB and closely related orthologs from the genus *Xanthomonas*. Although the calcium-binding site is not directly involved in the formation of the active site, its strategic position has an important role in the stabilization of interfacial loops comprising the −1 and −2 subsites. It was supported by molecular dynamics simulations, in which those residues forming the $\beta2$-$\alpha2$ (region I) and $\beta3$-$\alpha3$ (region II) loops (Fig. 14*B*) showed high RMSD values in the absence of calcium (Fig. 14*C*). Other residues forming the glycone-binding region, such as His^{92}, Asn^{137}, and Trp^{288}, also presented higher RMSD values without calcium ion (Fig. 14*A*), although they are not found in the $\beta2$-$\alpha2$ or $\beta3$-$\alpha3$ loops. These analyses indicate that the presence of calcium ion is structurally relevant for maintaining the active site geometry and that perturbations in this region might affect substrate recognition and binding.

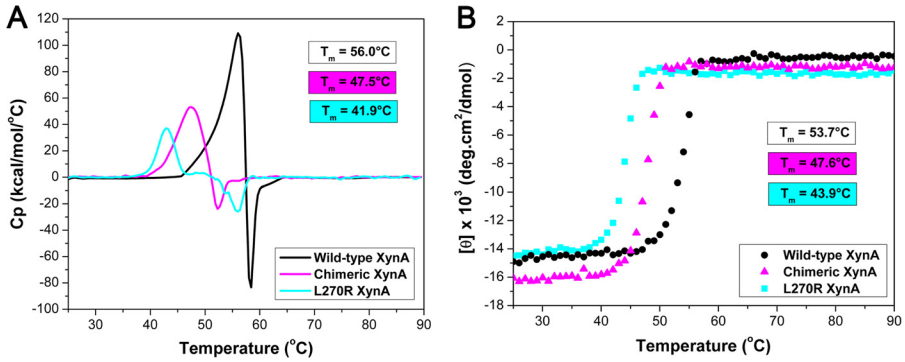

FIGURE 9. **Thermal stability of XynA constructs.** *A* and *B*, thermal denaturation profiles of WT, L270R, and chimeric XynA assessed by differential scanning calorimetry (*A*) and circular dichroism (*B*) experiments. The T_m calculated for each protein in each experiment is presented.

TABLE 4

Activity of XynB toward three xylose-based substrates

Xylan from beechwood is essentially a linear polymer of xylose (68). The xylosyl residues of arabinoxylans can be unsubstituted, monosubstituted via O_3 with arabinose residue, and disubstituted via O_3 and O_2 with arabinose residues. Rye arabinoxylan has 9% of xylosyl residues disubstituted and 35% monosubstituted, whereas wheat arabinoxylan has more disubstituted residues (20%) and fewer monosubstituted residues (14%) (69). The maximum relative activity (100%) corresponds to 401.4 units mg^{-1}.

Substrate	Relative activity
	%
Beechwood xylan	100
Rye arabinoxylan	86
Wheat arabinoxylan	38

DISCUSSION

Insights into GH10 Function and Evolution—It is a notable feature of the GH10 family that the glycone-binding region was preserved almost intact through the evolution, whereas the reducing end subsites have undergone profound changes for shaping the function of GH10 members in both prokaryotic and eukaryotic organisms. An inspection of the majority of GH10 structures available in the Protein Data Bank confirmed a conserved −2 and −1 subsites independent of their sequence similarity and mode of action as above indicated for Xac enzymes and homologs. In contrast, the aglycone-binding region is much divergent even among GH10 xylanases with sequence identity over 45%. Curiously, the most variable segment in this region is the loop connecting the β7 and α7 elements (Figs. 4, 5, and 11). XynA contains an insertion in this motif that induces dimerization and blocks the +2 subsite, whereas in CmXyn10B there is a long loop that participates in the formation of +2, +3, and +4 subsites. In other GH10 members, including XynB, TpXyl10B, and SoXyn10A, this loop is shortened and other loops, such as β6-α6 and β8-α8, participate in the formation of the aglycone-binding subsites. In TpXyl10B, it was demonstrated that conformational changes in the β8-α8 loop, induced by high temperatures, modify its mode of action (48). In addition to the distinct molecular architectures of the positive subsites among GH10 enzymes, the physicochemical basis for substrate binding is also variable. SoXyn10A interacts with the xylosyl residue at the +2 subsite by polar contacts, whereas in CmXyn10B it occurs by hydrophobic interactions. The subsites involved in the recognition of the aglycone region are so divergent that we were not able to map the subsites subsequent to +2 in XynB by structural

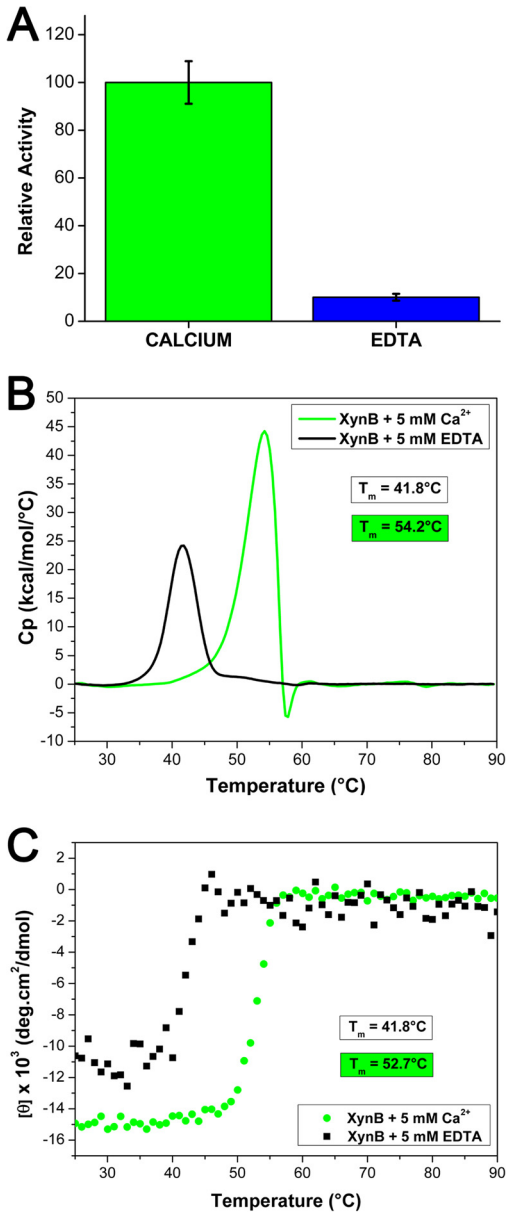

FIGURE 10. **The role of calcium ion in the enzymatic activity and structural stability of XynB.** *A*, the activity of XynB against beechwood xylan was drastically reduced in presence of EDTA. *B* and *C*, thermal stability of XynB in presence of calcium or EDTA assessed by differential scanning calorimetry (*B*) and circular dichroism (*C*) experiments. The T_m calculated for XynB in each experimental condition is shown.

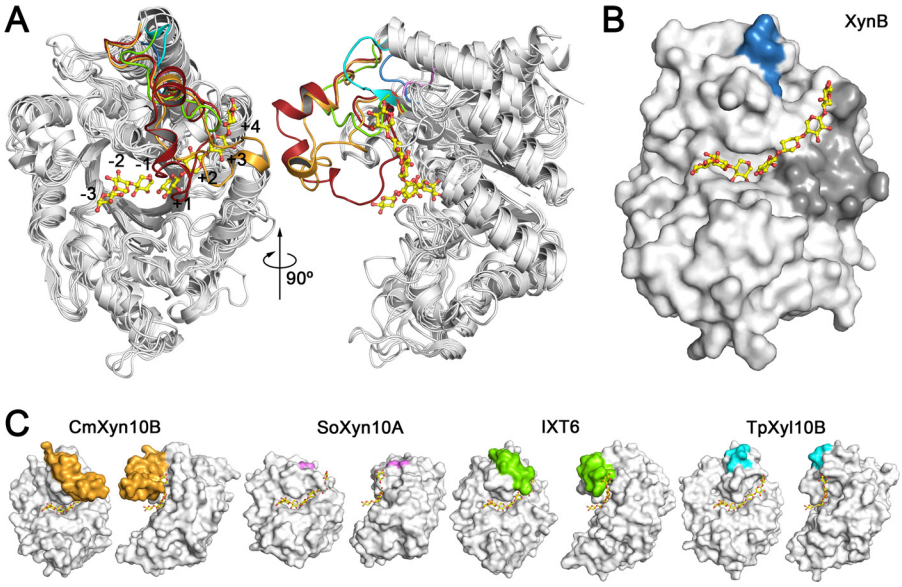

FIGURE 11. **Structural comparison of XynB with other structurally characterized GH10 xylanases.** *A*, superposition of XynA (Protein Data Bank code 4PMV; this work), CmXyn10B (Protein Data Bank code 1UQY (40)), SoXyn10A (Protein Data Bank code 1ISV (47)), IXT6 (Protein Data Bank code 2Q8X (41)), and TpXyl10B (Protein Data Bank code 3NIY (48)) structures on XynB (Protein Data Bank code 4PMX; this work). *B* and *C*, molecular surface of xylanases shown in *A*, except XynA. The $\beta7$-$\alpha7$ loop, which is very diverse among GH10 members, has the same color pattern in *A–C*. The oligosaccharide shown in *A–C* is from the CmXyn10B-complex structure (Protein Data Bank code 1UQY (40)). The *gray* color of XynB surface (*B*) indicates the divergent region in the positive subsites that in other xylanases is occupied by the loop Val^{136}–Trp^{166}.

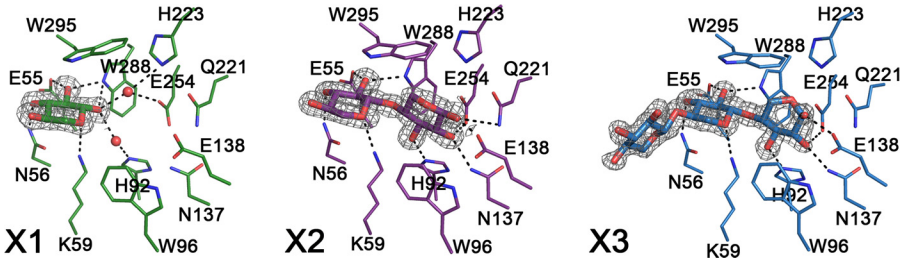

FIGURE 12. **XynB-xylooligosaccharides complexes.** The residues of the glycone-binding region of XynB are displayed, and the polar interactions with the carbohydrates are labeled. Electron density maps of xylose (X1), xylobiose (X2), and xylotriose (X3) in complex with XynB (Protein Data Bank codes 4PMY, 4PMZ, and 4PN2, respectively) are shown.

homology. In summary, structural and functional data available for GH10 xylanases, including our new findings regarding the Xac enzymes, support a common molecular recognition of the glycone region consisting basically of the −2 and −1 subsites. Moreover, it points to a large variability of the positive subsites, even among highly similar GH10 enzymes, becoming unpredictable changes in this region for driving the functional behavior, catalytic efficiency, or action mode of GH10 members.

Biological Implications: How GH10 Enzymes Contribute to Pathogenesis and Growth—A number of defense mechanisms have evolved in plants to prevent infection by pathogenic microorganisms (54–57). Many of phytopathogenic fungi produce a rich repertoire of CWDEs such as cellulases and xylanases to assist their colonization and for nutrient uptake (58–60). However, the oligosaccharides that are generated by these enzymes are sensed by plants and elicit the innate immune response (22). Other mechanism for plant resistance is the production of protein inhibitors of glucanases that directly affects the pathogenesis (61, 62). *Xanthomonas* spp. have a complete arsenal of CWDEs, but their putative roles in pathogenesis and pathogen-host interactions remain largely unknown. Here, we have elucidated the functional and structural properties of the two major GH10 xylanase-related proteins found in Xac serving as a model to understand the molecular events associated with xylan degradation and pathogenesis. The divergent XynB proved to be the primary xylanolytic enzyme, being an important component for hemicellulose degradation, a key constituent of the plant cell wall (Fig. 15). The breakdown of such polysaccharides is probably related to nutrient uptake, and the impairment of plant cell wall integrity may represent an advantage for the pathogen, facilitating the assembly of T3SS and consequently the translocation of effector proteins (Fig. 15). Indeed, several T2SS genes from *Xanthomonas* spp., mostly CWDEs, are coregulated with T3SS elements, supporting this model (14–16). However, the plant cell wall damage can be considered a double-edged sword because it not only serves as a point of entry to the phytopathogen or even a way for translocation of effector molecules, but also as a signaling mechanism, triggering host defense responses (11). Interestingly, some plant pathogens have evolved molecular strategies to suppress such innate immune responses elicited by oligosaccharides produced by the action of CWDEs (7, 63). The fact of XynA degrades xylooligosaccharides derived from xylan breakdown by XynB may suggest that this novel GH10 enzyme makes part

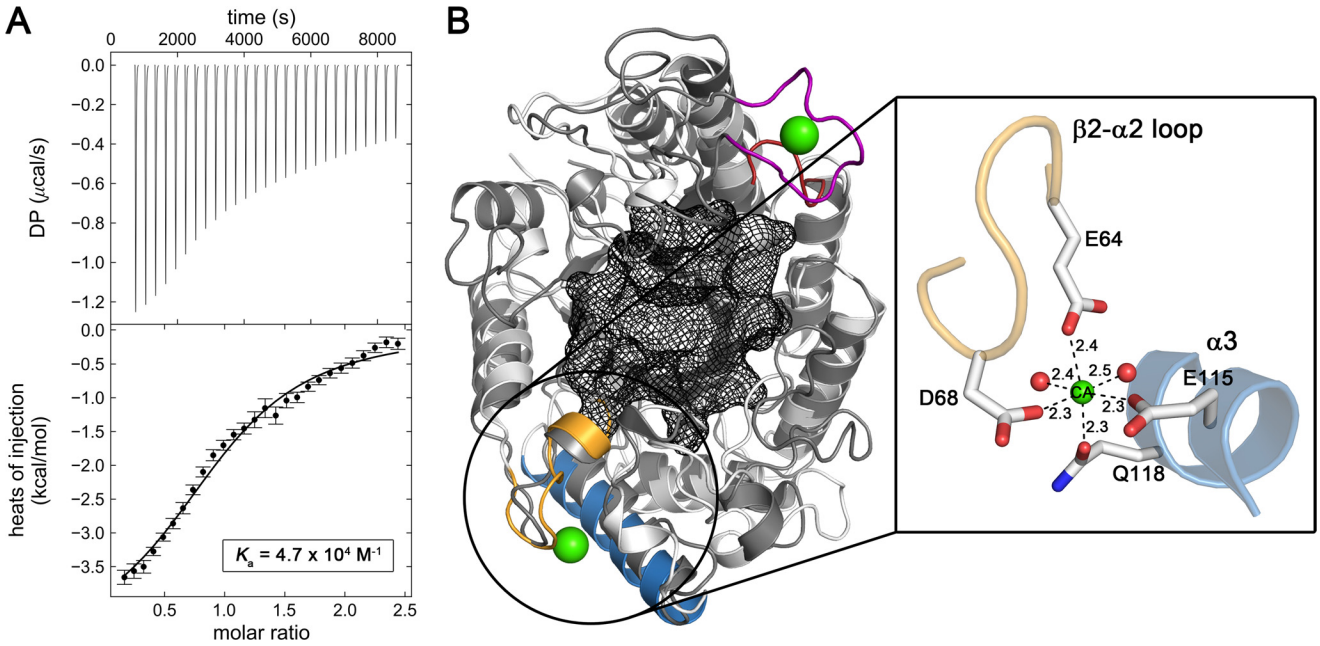

FIGURE 13. **The calcium-binding site of XynB.** *A*, isothermal titration calorimetry measurements with calcium titration. The *DP* is a measured power differential between the reference and sample cells necessary to maintain their temperature difference at close to zero. *B*, superposition of CjXylA structure (*gray*, Protein Data Bank code 1CLX (66)) on XynB structure (*white*, Protein Data Bank code 4PMX; this work). The regions that form the calcium-binding site of CjXylA are colored in *red* and *pink*. The regions that form the calcium-binding site of XynB are colored in *blue* and *orange*. The catalytic groove of XynB is delineated as a *black mesh*. The calcium coordination sphere in the XynB structure is shown in detail (*boxed area*).

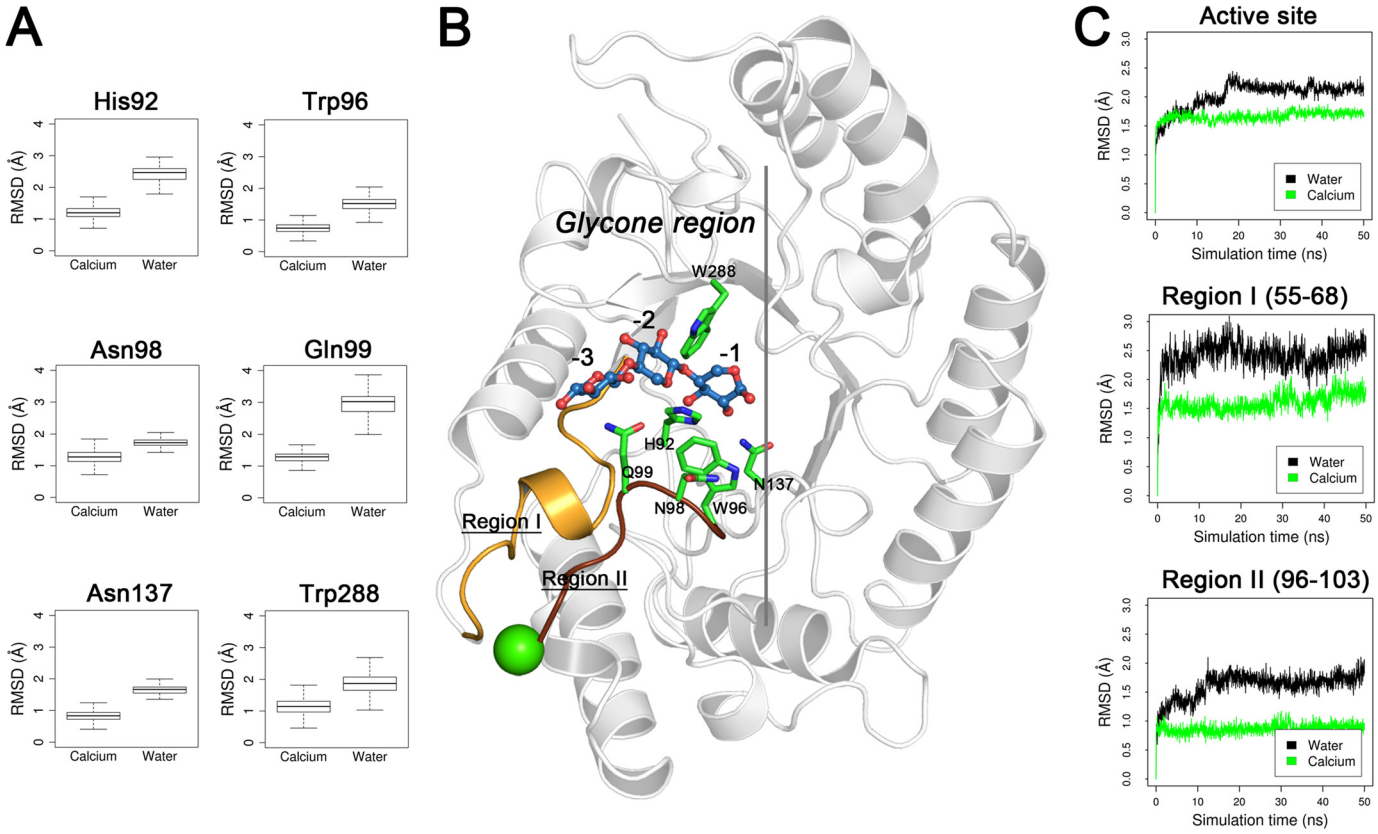

FIGURE 14. **Molecular dynamics simulations of XynB in presence or absence of calcium.** *A*, residues forming the negative subsites that were perturbed upon calcium removal. *B*, structure of XynB showing the relative position of calcium ion, regions I and II, and critical residues shown in *A*. The oligosaccharide is from XynB complex structure (Protein Data Bank code 4PN2) and is shown to indicate the glycone-binding region. *C*, RMSD analysis of entire active site cleft and regions I and II. Although the calcium ion is not directly bound to the residues forming the glycone-binding region, these results indicate that the destabilizing effect upon calcium removal is propagated to the active site through the regions I and II, being detrimental to substrate recognition and consequently to catalytic activity.

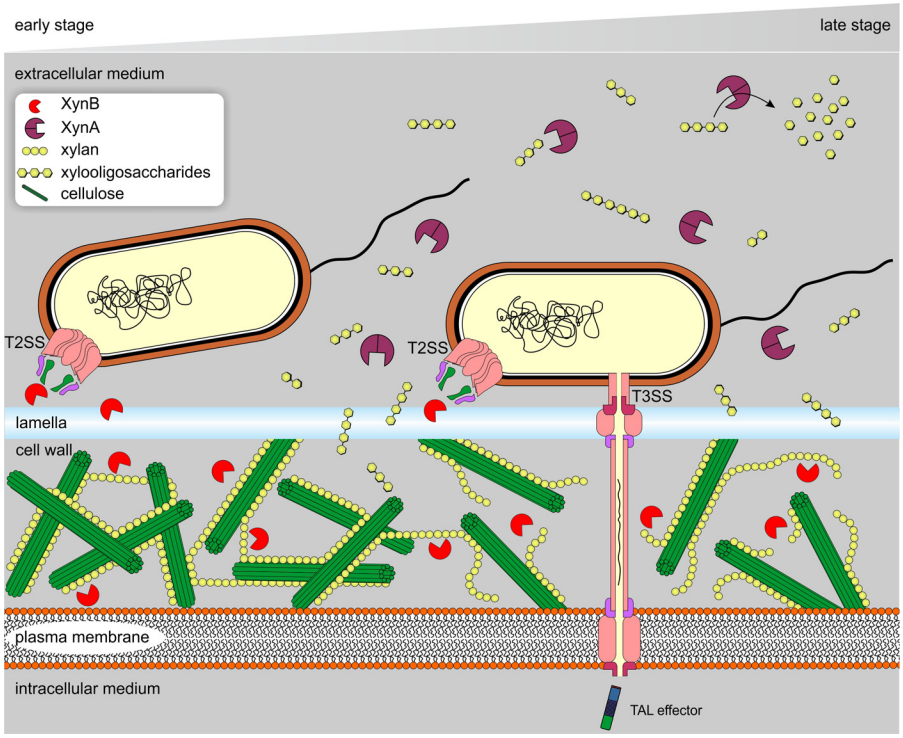

FIGURE 15. **Schematic representation of the roles played by XynA and XynB during *Xanthomonas* infection and pathogenesis.** At an early stage, the T2SS secretes a number of glycoside hydrolases including XynA and XynB. XynB has a primary role in degrading the hemicellulosic fraction of the plant cell wall that is important for nutrient uptake and for breaching the first physical barrier against the bacterial attack. The weakened cell wall facilitates the insertion of T3SS, responsible for delivering effector proteins and other molecules into the plant cytoplasmatic environment, illustrating the interplay between T2SS and T3SS. At the late stage, the soluble xylooligosaccharides released by the action of XynB are elicitors of the innate immune system and then XynA with its reducing end xylose-releasing exo-oligoxylanase activity sequesters and cleaves them into xylose units, contributing to suppress the development of a systemic response.

of the *Xanthomonas* strategy to suppress oligosaccharide-induced defense responses (Fig. 15). A similar suppression mechanism was already observed for other phytopathogens, however, involving chitinase-like proteins (63). In addition, we are tempted to speculate that the dimerization of XynA and the very low sequence identity of XynB to GH10 xylanases from other phytopathogens, principally fungi that are typical cell wall-degrading organisms, are a camouflage mechanism to prevent their recognition by plant receptors and inhibitors. These findings and interpretations indicate potential novel molecular mechanisms associated to plant-*Xanthomonas* interaction and provide clues of how this pathogen has evolved sophisticated strategies to overcome the host defense responses.

Biotechnological Implications: New Routes for Xylan Degradation—Some saprotrophic microorganisms, such as the fungus *Trichoderma reesei*, produce a broad arsenal of CWDEs to degrade plant biomass, and their enzymes have been successfully employed in biotechnological processes (64). However, phytopathogens like *Xanthomonas* spp., which infect plants through stomata and lesions (18, 19), intriguingly also contains a large number of CWDEs. Xac, for instance, contains at least 160 genes related to carbohydrate modification and degradation spread into 44 GH families, which is comparable in number to fungi specialized in plant cell wall degradation such as *Aspergillus niger* and *Neurospora crassa* (CAZy database (17)). Although these bacteria represent a rich source for prospecting novel enzymes with biotechnological applications, very few GH enzymes from *Xanthomonas* have been structurally and functionally investigated. Herein, our studies revealed unique mechanisms associated with xylan degradation such as the reducing end xylose-releasing exo-oligoxylanase activity of XynA and the calcium stimulation of XynB. In addition, the chimeric XynA, redesigned based on endo-xylanases, showed high catalytic efficiency, being a promising engineered enzyme for bioprocesses at moderate temperature such as simultaneous saccharification and fermentation for bioethanol production (65). These findings reveal new molecular strategies for plant cell wall deconstruction, broadening our knowledge about the activities and regulatory mechanisms found in the GH10 family and highlighting the great potential of plant bacterial pathogens as a source of biotechnologically relevant enzymes.

Acknowledgments—We are thankful to Brazilian Synchrotron Light Laboratory and Brazilian Biosciences National Laboratory for the provision of time on the MX2, SAXS1, and SAXS2 Beamlines, and both crystallization (Robolab) and spectroscopy (LEC) facilities.

REFERENCES

1. Ray, S. K., Rajeshwari, R., and Sonti, R. V. (2000) Mutants of *Xanthomonas oryzae* pv. oryzae deficient in general secretory pathway are virulence deficient and unable to secrete xylanase. *Mol. Plant. Microbe Interact.* **13,** 394–401
2. Hu, J., Qian, W., and He, C. (2007) The *Xanthomonas oryzae* pv. oryzae eglXoB endoglucanase gene is required for virulence to rice. *FEMS Microbiol. Lett.* **269,** 273–279
3. Rajeshwari, R., Jha, G., and Sonti, R. V. (2005) Role of an in planta-expressed xylanase of *Xanthomonas oryzae* pv. oryzae in promoting viru-

lence on rice. *Mol. Plant. Microbe Interact.* **18,** 830–837
4. Albersheim, P., Jones, T. M., and English, P. D. (1969) Biochemistry of the cell wall in relation to infective processes. *Annu. Rev. Phytopathol.* **7,** 171–194
5. Büttner, D., and Bonas, U. (2010) Regulation and secretion of *Xanthomonas* virulence factors. *FEMS Microbiol. Rev.* **34,** 107–133
6. Preston, G. M., Studholme, D. J., and Caldelari, I. (2005) Profiling the secretomes of plant pathogenic Proteobacteria. *FEMS Microbiol. Rev.* **29,** 331–360
7. Jha, G., Rajeshwari, R., and Sonti, R. V. (2005) Bacterial type two secretion system secreted proteins: double-edged swords for plant pathogens. *Mol. Plant. Microbe Interact.* **18,** 891–898
8. Enkerli, J., Felix, G., and Boller, T. (1999) The enzymatic activity of fungal xylanase is not necessary for its elicitor activity. *Plant Physiol.* **121,** 391–397
9. Furman-Matarasso, N., Cohen, E., Du, Q., Chejanovsky, N., Hanania, U., and Avni, A. (1999) A point mutation in the ethylene-inducing xylanase elicitor inhibits the beta-1–4-endoxylanase activity but not the elicitation activity. *Plant Physiol.* **121,** 345–351
10. Hanania, U., and Avni, A. (1997) High-affinity binding site for ethylene-inducing xylanase elicitor on Nicotiana tabacum membranes. *Plant J.* **12,** 113–120
11. Ryan, C. A. (1987) Oligosaccharide signalling in plants. *Annu. Rev. Cell Biol.* **3,** 295–317
12. Fry, S. C., Aldington, S., Hetherington, P. R., and Aitken, J. (1993) Oligosaccharides as signals and substrates in the plant cell wall. *Plant Physiol.* **103,** 1–5
13. Palva, T. K., Holmstrom, K.-O., Heino, P., and Palva, E. T. (1993) Induction of plant defense response by exoenzymes of *Erwinia carotovora* subsp. carotovora. *Mol. Plant. Microbe Interact.* **6,** 190–196
14. Szczesny, R., Jordan, M., Schramm, C., Schulz, S., Cogez, V., Bonas, U., and Büttner, D. (2010) Functional characterization of the Xcs and Xps type II secretion systems from the plant pathogenic bacterium *Xanthomonas campestris* pv. vesicatoria. *New Phytol.* **187,** 983–1002
15. Jha, G., Rajeshwari, R., and Sonti, R. V. (2007) Functional interplay between two *Xanthomonas oryzae* pv,. oryzae secretion systems in modulating virulence on rice. *Mol. Plant. Microbe Interact.* **20,** 31–40
16. Yamazaki, A., Hirata, H., and Tsuyumu, S. (2008) HrpG regulates type II secretory proteins in *Xanthomonas axonopodis* pv. citri. *J. Gen. Plant Pathol.* **74,** 138–150
17. Lombard, V., Golaconda Ramulu, H., Drula, E., Coutinho, P. M., and Henrissat, B. (2014) The carbohydrate-active enzymes database (CAZy) in 2013. *Nucleic Acids Res.* **42,** D490–D495
18. Gottwald, T. R., and Graham, J. H. (1992) A device for precise and non-disruptive stomatal inoculation of leaf tissue with bacterial pathogens. *Phytopathology* **82,** 930–935
19. Graham, J. H., Gottwald, T. R., Riley, T. D., and Achor, D. (1992) Penetration through leaf stomata and strains of *Xanthomonas campestris* in citrus cultivars varying in susceptibility to bacterial diseases. *Phytopathology* **82,** 1319–1325
20. Déjean, G., Blanvillain-Baufumé, S., Boulanger, A., Darrasse, A., Dugé de Bernonville, T., Girard, A. L., Carrére, S., Jamet, S., Zischek, C., Lautier, M., Solé, M., Büttner, D., Jacques, M. A., Lauber, E., and Arlat, M. (2013) The xylan utilization system of the plant pathogen *Xanthomonas campestris* pv. campestris controls epiphytic life and reveals common features with oligotrophic bacteria and animal gut symbionts. *New Phytol.* **198,** 899–915
21. Li, J., and Wang, N. (2011) Genome-wide mutagenesis of *Xanthomonas axonopodis* pv. citri reveals novel genetic determinants and regulation mechanisms of biofilm formation. *PLoS One* **6,** e21804
22. Shibuya, N., and Minami, E. (2001) Oligosaccharide signalling for defence responses in plant. *Physiol. Mol. Plant Pathol.* **59,** 223–233
23. Miller, G. L. (1959) Use of dinitrosalicylic acid reagent for determination of reducing sugar. *Anal. Chem.* **31,** 426–428
24. Chen, F. T., and Evangelista, R. A. (1995) Analysis of mono- and oligosaccharide isomers derivatized with 9-aminopyrene-1,4,6-trisulfonate by capillary electrophoresis with laser-induced fluorescence. *Anal. Biochem.* **230,** 273–280
25. Keller, S., Vargas, C., Zhao, H., Piszczek, G., Brautigam, C. A., and Schuck, P. (2012) High-precision isothermal titration calorimetry with automated peak-shape analysis. *Anal. Chem.* **84,** 5066–5073
26. Hammersley, A. P., Brown, K., Burmeister, W., Claustre, L., Gonzalez, A., McSweeney, S., Mitchell, E., Moy, J. P., Svensson, S. O., and Thompson, A. W. (1997) Calibration and application of an x-ray image intensifier/charge-coupled device detector for monochromatic macromolecular crystallography. *J. Synchrotron Radiat.* **4,** 67–77
27. Svergun, D. (1992) Determination of the regularization parameter in indirect-transform methods using perceptual criteria. *J. Appl. Crystallogr.* **25,** 495–503
28. Svergun, D. I. (1999) Restoring low resolution structure of biological macromolecules from solution scattering using simulated annealing. *Biophys. J.* **76,** 2879–2886
29. Volkov, V. V., and Svergun, D. I. (2003) Uniqueness of *ab initio* shape determination in small-angle scattering. *J. Appl. Crystallogr.* **36,** 860–864
30. Svergun, D., Barberato, C., and Koch, M. H. J. (1995) CRYSOL: a program to evaluate x-ray solution scattering of biological macromolecules from atomic coordinates. *J. Appl. Crystallogr.* **28,** 768–773
31. Kozin, M. B., and Svergun, D. I. (2001) Automated matching of high- and low-resolution structural models. *J. Appl. Crystallogr.* **34,** 33–41
32. Otwinowski, Z., and Minor, W. (1997) Processing of x-ray diffraction data collected in oscillation mode. *Methods Enzymol.* **276,** 307–326
33. Kabsch, W. (2010) XDS. *Acta Crystallogr. D. Biol. Crystallogr.* **66,** 125–132
34. Sheldrick, G. M. (2010) Experimental phasing with SHELXC/D/E: combining chain tracing with density modification. *Acta Crystallogr. D. Biol. Crystallogr.* **66,** 479–485
35. Terwilliger, T. C., Grosse-Kunstleve, R. W., Afonine, P. V., Moriarty, N. W., Zwart, P. H., Hung, L. W., Read, R. J., and Adams, P. D. (2008) Iterative model building, structure refinement and density modification with the PHENIX AutoBuild wizard. *Acta Crystallogr. D. Biol. Crystallogr.* **64,** 61–69
36. Afonine, P. V., Grosse-Kunstleve, R. W., Echols, N., Headd, J. J., Moriarty, N. W., Mustyakimov, M., Terwilliger, T. C., Urzhumtsev, A., Zwart, P. H., and Adams, P. D. (2012) Towards automated crystallographic structure refinement with phenix.refine. *Acta Crystallogr. D. Biol. Crystallogr.* **68,** 352–367
37. Emsley, P., Lohkamp, B., Scott, W. G., and Cowtan, K. (2010) Features and development of Coot. *Acta Crystallogr. D. Biol. Crystallogr.* **66,** 486–501
38. Chen, V. B., Arendall, W. B., 3rd, Headd, J. J., Keedy, D. A., Immormino, R. M., Kapral, G. J., Murray, L. W., Richardson, J. S., and Richardson, D. C. (2010) MolProbity: all-atom structure validation for macromolecular crystallography. *Acta Crystallogr. D Biol. Crystallogr.* **66,** 12–21
39. Krieger, E., Koraimann, G., and Vriend, G. (2002) Increasing the precision of comparative models with YASARA NOVA: a self-parameterizing force field. *Proteins* **47,** 393–402
40. Pell, G., Taylor, E. J., Gloster, T. M., Turkenburg, J. P., Fontes, C. M., Ferreira, L. M., Nagy, T., Clark, S. J., Davies, G. J., and Gilbert, H. J. (2004) The mechanisms by which family 10 glycoside hydrolases bind decorated substrates. *J. Biol. Chem.* **279,** 9597–9605
41. Solomon, V., Teplitsky, A., Shulami, S., Zolotnitsky, G., Shoham, Y., and Shoham, G. (2007) Structure-specificity relationships of an intracellular xylanase from *Geobacillus stearothermophilus*. *Acta Crystallogr. D. Biol. Crystallogr.* **63,** 845–859
42. Gallardo, O., Pastor, F. I., Polaina, J., Diaz, P., Lysek, R., Vogel, P., Isorna, P., González, B., and Sanz-Aparicio, J. (2010) Structural insights into the specificity of Xyn10B from *Paenibacillus barcinonensis* and its improved stability by forced protein evolution. *J. Biol. Chem.* **285,** 2721–2733
43. Honda, Y., and Kitaoka, M. (2004) A family 8 glycoside hydrolase from *Bacillus halodurans* C-125 (BH2105) is a reducing end xylose-releasing exo-oligoxylanase. *J. Biol. Chem.* **279,** 55097–55103
44. Fushinobu, S., Hidaka, M., Honda, Y., Wakagi, T., Shoun, H., and Kitaoka, M. (2005) Structural basis for the specificity of the reducing end xylose-releasing exo-oligoxylanase from *Bacillus halodurans* C-125. *J. Biol. Chem.* **280,** 17180–17186
45. Mirande, C., Mosoni, P., Béra-Maillet, C., Bernalier-Donadille, A., and Forano, E. (2010) Characterization of Xyn10A, a highly active xylanase from the human gut bacterium *Bacteroides xylanisolvens* XB1A. *Appl.*

Microbiol. Biotechnol. **87,** 2097–2105
46. Guo, B., Chen, X. L., Sun, C. Y., Zhou, B. C., and Zhang, Y. Z. (2009) Gene cloning, expression and characterization of a new cold-active and salt-tolerant endo-β-1,4-xylanase from marine *Glaciecola mesophila* KMM 241. *Appl. Microbiol. Biotechnol.* **84,** 1107–1115
47. Fujimoto, Z., Kuno, A., Kaneko, S., Kobayashi, H., Kusakabe, I., and Mizuno, H. (2002) Crystal structures of the sugar complexes of *Streptomyces olivaceoviridis* E-86 xylanase: sugar binding structure of the family 13 carbohydrate binding module. *J. Mol. Biol.* **316,** 65–78
48. Santos, C. R., Meza, A. N., Hoffmam, Z. B., Silva, J. C., Alvarez, T. M., Ruller, R., Giesel, G. M., Verli, H., Squina, F. M., Prade, R. A., and Murakami, M. T. (2010) Thermal-induced conformational changes in the product release area drive the enzymatic activity of xylanases 10B: crystal structure, conformational stability and functional characterization of the xylanase 10B from *Thermotoga petrophila* RKU-1. *Biochem. Biophys. Res. Commun.* **403,** 214–219
49. Shi, H., Zhang, Y., Li, X., Huang, Y., Wang, L., Wang, Y., Ding, H., and Wang, F. (2013) A novel highly thermostable xylanase stimulated by Ca^{2+} from *Thermotoga thermarum*: cloning, expression and characterization. *Biotechnol. Biofuels* **6,** 26
50. Spurway, T. D., Morland, C., Cooper, A., Sumner, I., Hazlewood, G. P., O'Donnell, A. G., Pickersgill, R. W., and Gilbert, H. J. (1997) Calcium protects a mesophilic xylanase from proteinase inactivation and thermal unfolding. *J. Biol. Chem.* **272,** 17523–17530
51. Wang, G., Luo, H., Wang, Y., Huang, H., Shi, P., Yang, P., Meng, K., Bai, Y., and Yao, B. (2011) A novel cold-active xylanase gene from the environmental DNA of goat rumen contents: direct cloning, expression and enzyme characterization. *Bioresour. Technol.* **102,** 3330–3336
52. Zheng, H., Chordia, M. D., Cooper, D. R., Chruszcz, M., Müller, P., Sheldrick, G. M., and Minor, W. (2014) Validation of metal-binding sites in macromolecular structures with the CheckMyMetal web server. *Nat. Protoc.* **9,** 156–170
53. Najmudin, S., Pinheiro, B. A., Prates, J. A., Gilbert, H. J., Romão, M. J., and Fontes, C. M. (2010) Putting an N-terminal end to the *Clostridium thermocellum* xylanase Xyn10B story: crystal structure of the CBM22–1-GH10 modules complexed with xylohexaose. *J. Struct. Biol.* **172,** 353–362
54. Grennan, A. K. (2006) Plant response to bacterial pathogens. Overlap between innate and gene-for-gene defense response. *Plant Physiol.* **142,** 809–811
55. Broekaert, W. F., Terras, F. R., Cammue, B. P., and Osborn, R. W. (1995) Plant defensins: novel antimicrobial peptides as components of the host defense system. *Plant Physiol.* **108,** 1353–1358
56. Veronese, P., Ruiz, M. T., Coca, M. A., Hernandez-Lopez, A., Lee, H., Ibeas, J. I., Damsz, B., Pardo, J. M., Hasegawa, P. M., Bressan, R. A., and Narasimhan, M. L. (2003) In defense against pathogens: both plant sentinels and foot soldiers need to know the enemy. *Plant Physiol.* **131,** 1580–1590
57. Liu, Y., Schiff, M., Czymmek, K., Tallóczy, Z., Levine, B., and Dinesh-Kumar, S. P. (2005) Autophagy regulates programmed cell death during the plant innate immune response. *Cell* **121,** 567–577
58. Van Vu, B., Itoh, K., Nguyen, Q. B., Tosa, Y., and Nakayashiki, H. (2012) Cellulases belonging to glycoside hydrolase families 6 and 7 contribute to the virulence of Magnaporthe oryzae. *Mol. Plant. Microbe Interact.* **25,** 1135–1141
59. Faure, D. (2002) The family-3 glycoside hydrolases: from housekeeping functions to host-microbe interactions. *Appl. Environ. Microbiol.* **68,** 1485–1490
60. King, B. C., Waxman, K. D., Nenni, N. V., Walker, L. P., Bergstrom, G. C., and Gibson, D. M. (2011) Arsenal of plant cell wall degrading enzymes reflects host preference among plant pathogenic fungi. *Biotechnol. Biofuels* **4,** 4
61. Fierens, K., Gils, A., Sansen, S., Brijs, K., Courtin, C. M., Declerck, P. J., De Ranter, C. J., Gebruers, K., Rabijns, A., Robben, J., Campenhout, S., Volckaert, G., and Delcour, J. A. (2005) His374 of wheat endoxylanase inhibitor TAXI-I stabilizes complex formation with glycoside hydrolase family 11 endoxylanases. *FEBS J.* **272,** 5872–5882
62. Yoshizawa, T., Shimizu, T., Hirano, H., Sato, M., and Hashimoto, H. (2012) Structural basis for inhibition of xyloglucan-specific endo-β-1,4-glucanase (XEG) by XEG-protein inhibitor. *J. Biol. Chem.* **287,** 18710–18716
63. de Jonge, R., van Esse, H. P., Kombrink, A., Shinya, T., Desaki, Y., Bours, R., van der Krol, S., Shibuya, N., Joosten, M. H., and Thomma, B. P. (2010) Conserved fungal LysM effector Ecp6 prevents chitin-triggered immunity in plants. *Science* **329,** 953–955
64. Schuster, A., and Schmoll, M. (2010) Biology and biotechnology of *Trichoderma*. *Appl. Microbiol. Biotechnol.* **87,** 787–799
65. Doran-Peterson, J., Jangid, A., Brandon, S. K., DeCrescenzo-Henriksen, E., Dien, B., and Ingram, L. O. (2009) Simultaneous saccharification and fermentation and partial saccharification and co-fermentation of lignocellulosic biomass for ethanol production. *Methods Mol. Biol.* **581,** 263–280
66. Harris, G. W., Jenkins, J. A., Connerton, I., and Pickersgill, R. W. (1996) Refined crystal structure of the catalytic domain of xylanase A from *Pseudomonas fluorescens* at 1.8 A resolution. *Acta Crystallogr. D. Biol. Crystallogr.* **52,** 393–401
67. Tina, K. G., Bhadra, R., and Srinivasan, N. (2007) PIC: protein interactions calculator. *Nucleic Acids Res.* **35,** W473–W476
68. Hespell, R. B., and Cotta, M. A. (1995) Degradation and utilization by *Butyrivibrio fibrisolvens* H17c of xylans with different chemical and physical properties. *Appl. Environ. Microbiol.* **61,** 3042–3050
69. Dervilly-Pinel, G., Thibault, J. F., and Saulnier, L. (2001) Experimental evidence for a semi-flexible conformation for arabinoxylans. *Carbohydr. Res.* **330,** 365–372